Three-dimensional Whole-body Small animal Photoacoustic Tomography using a Multi-view Fabry-Perot scanner

Olumide Ogunlade, Robert Ellwood, Edward Zhang, Benjamin T Cox and Paul Beard

Abstract—**Photoacoustic tomography (PAT) has the potential to become a widely used imaging tool in preclinical studies of small animals. This is because it can provide non-invasive, label free images of whole-body mouse anatomy, in a manner which is challenging for more established imaging modalities. However, existing PAT scanners are limited because they either do not implement a full 3-D tomographic reconstruction using all the recorded photoacoustic (PA) data and/or do not record the available 3-D PA time-series data around the mouse with sufficiently high spatial resolution (~100µm), which compromises image quality in terms of resolution, imaging depth and the introduction of artefacts. In this study, we address these limitations by demonstrating an all-optical, multi-view Fabry-Perot based scanner for whole body small animal imaging. The scanner densely samples the acoustic field with a large number of detection points (>100,000), evenly distributed around the mouse. The locations of the detection points were registered onto a common coordinate system, before a tomographic reconstruction using all the recorded PA time series was implemented. This enabled the acquisition of high resolution, whole-body PAT images of ex-vivo mice, with anatomical features visible across the entire cross section.**

Index Terms—**Photoacoustic tomography, Whole-body imaging, Computed tomography, Image reconstruction, Image registration.**

I. INTRODUCTION

Preclinical studies of small animals, such as rodents, are important in the development of new medicines. For example, to determine the toxicity profile and bio-distribution of a new drug, mice are used to study its toxicological characteristics and its accumulation in various organs in the body. For these studies, non-invasive, harmless, imaging techniques are attractive because they enable visualisation of the whole mouse anatomy in a longitudinal manner. Photoacoustic tomography (PAT) is a promising technique for this application, because it provides label free, high resolution, three-dimensional images based on optical absorption contrast, whilst overcoming limitations associated with more established techniques, such as the need for exogenous contrast agents (MRI), poor spatial resolution (PET) and the use of ionising radiation (micro-CT) [1].

In PAT, ultrasound waves are generated when a large diameter pulsed laser beam is used to irradiate tissue with wide-field illumination [2]. The light is absorbed by chromophores within the tissue, and the subsequent thermalisation of the energy gives rise to a spatially-varying excess pressure. The pressure, called the 'initial acoustic pressure distribution', becomes the source of broadband acoustic waves which propagate to the tissue surface where they are detected by an array of ultrasound receivers. The aim of PAT is to image this initial acoustic pressure distribution, because it is closely related to the tissue chromophore distribution and therefore carries information about the tissue structure and function.

In order to form a high quality, whole-body 3-D PAT image, it is essential to capture all the available acoustic data with high fidelity. There are several ways in which a PAT scanner might fail to do this: (a) The data is not recorded over a 360-degree angular aperture around the mouse, called 'limited-view' detection; (b) Spatial undersampling of the data, usually because of hardware constraints, e.g. the limited element density of piezoelectric arrays; (c) The use of ultrasound detectors which have a limited angular detection range, often as a result of using a large detection area to obtain sufficient sensitivity to detect the weak photoacoustic signals, and (d) The use of ultrasound detectors which cannot capture the full bandwidth of photoacoustic waves.

Whole-body piezoelectric-based 3D PAT scanners that have been demonstrated to date do not meet one or more of these requirements. This has limited the image quality achievable, in terms of the image resolution, imaging depth and the

introduction of artefacts. In studies where the acoustic data was recorded from only one side of the mouse, the imaging depth was insufficient for visualising the entire mouse cross section [3-5]. This limitation has been addressed by enclosing the mouse with a 1D ring array of detectors that are weakly focused in the elevational direction [6,7]. A whole-body 3D image can then be obtained by axially scanning the array, reconstructing a 2D cross-sectional image at each axial position and stacking the reconstructed images together. However, the weak elevational focusing of the detectors results in significantly poorer resolution in the axial direction than radially, and there is greater risk of out-of-plane artifacts with this approach. Reconstructing the image from time-series data recorded using an array of omnidirectional detectors that surrounds the mouse avoids this limitation. Scanners based on this type of full 3-D tomographic reconstruction approach have been reported based on the rotation of an arc shaped array[8-9] or a spherical matrix array [10]. However, the total number of the detector elements used (~10,000), and their uneven distribution around the mouse, resulted in spatial under-sampling of the acoustic field in one or more directions. Indeed, this is a common feature of previous studies. Spatial sampling must meet the spatial Nyquist criterion, in order to avoid aliasing. For example, the isotropic spatial sampling interval should be $\leq$ 100 μm to accurately record acoustic frequencies up to 7.5MHz, which are required for high resolution imaging (assuming detectors placed close to the mouse, and a sound speed of 1500 m s^{-1}). To achieve this requires of the order of 100,000 evenly placed transducer elements around the mouse, which is challenging to achieve with the piezoelectric sensors used in previous studies; the typical element size and inter element spacing were of the order of mms and several 100s of micometers respectively.

To address these limitations, we describe a whole-body scanner based on a Fabry-Perot (FP) ultrasound sensor. This offers two key advantages. Firstly, it acquires full-view 2-D data over a 360-degree angular aperture and all of this data is used to form a whole-body image of the mouse via a full 3-D tomographic reconstruction; it thus avoids the poor elevational resolution and the artefacts associated with the use of weakly focused ring arrays. Secondly, unlike piezoelectric sensors, the FP ultrasound sensor is capable of fine sampling of acoustic fields at MHz frequencies, due to its small optically defined element size (~60μm) [11] and interelement spacing (~100μm). In addition, it offers high sensitivity relative to the element size and wide bandwidth, which is essential for accurate image reconstruction. Previously, it has been shown that a planar FP-sensor based scanner can provide detailed images of mouse anatomy [12-14]. However, like all planar detection geometries, it has a limited-view of the acoustic field. This results in reconstruction artefacts and also limits the depth at which anatomical features can be visualised, thus making it unsuitable for whole-body imaging.

In this paper, we describe the operating principles of the scanner (referred to herein as multi-view) which works by synthesising eight notional planar detector arrays around the imaging target, achieved by rotating the target relative to a stationary FP sensor. A novel registration procedure is used to register the sensors, before a full 3-D tomographic reconstruction of the image is performed. The system has been

evaluated by imaging phantoms to determine its spatial resolution, field of view and image fidelity and compared to a single-view FP sensor scanner. To illustrate its applicability to whole-body small animal imaging, detailed volumetric PA images of the mouse anatomy were acquired.

II. MATERIALS AND METHODS
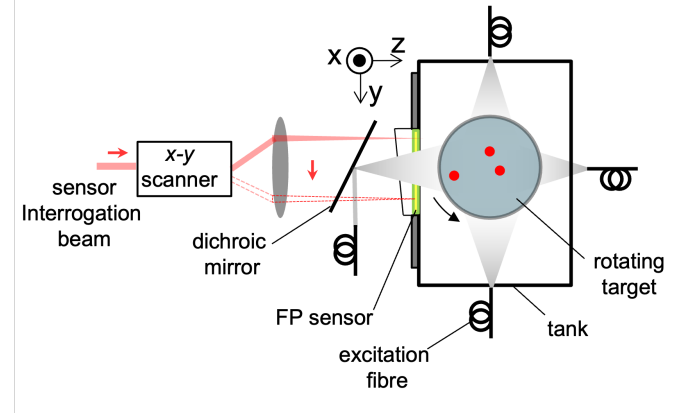
A. Experimental setup

Fig. 1. Schematic illustrating the operation of the multi-view FP sensor-based photoacoustic scanner. PA signals are generated by illuminating the target with a ~2.45cm diameter beam from four sides. The PA signals are detected using a stationary planar FP sensor. Multi-view imaging is achieved by rotating the target and acquiring PA signals in 8 views; equivalent to placing 8 FP sensors around the target.

The multi-view scanner is based on a planar FP ultrasound sensor, as shown in the schematic in Fig 1. The sensor operates by detecting the PA-induced modulation of the thickness of the sensor using a focussed interrogation beam [11]. In this study, a single interrogation beam was scanned over a sensor (*x-y*) surface area of 14 x 20 mm, in steps of 100μm or 120μm, thus synthesizing a 2-D array of ultrasound detectors. The thickness of the sensor was 22μm, with a 3dB bandwidth of 40MHz. The sensor was mounted flush with the inner surface of a tank filled with deionised water, into which the imaging target was immersed. The target was contained in a custom cylindrically-shaped sample holder, made from an optically and acoustically transparent 50μm thick polymer film mounted on an optical post. The sample holder was attached to a precision motorised rotating stage, with the axis of rotation located approximately 12 mm from the sensor. PA signals were generated by illuminating the target with the output of a tuneable pulsed OPO laser system (PhotoSonus M-20, Ekspla). The OPO output is coupled into a fibre bundle which fans out into four output arms. This enabled illumination of the target from four sides, including through the FP sensor in backward mode. The maximum pulse energy at the output of the fibre bundle was 120mJ which was distributed evenly over the four arms, for excitation wavelengths between 700 - 800nm used in this study. The laser light from each arm was delivered to the target in a 2.45cm diameter beam, resulting in an incident fluence of 6.4mJ cm^{-2} on each side. Depending on the scanned area and step size, between 10,000 - 20,000 waveforms were acquired using a digitiser without averaging. Each waveform contained

1200 points acquired at a sampling rate of 50 MHz. Multi-view data acquisition was achieved by rotating the imaging target in angular steps and performing an x-y scan of the FP sensor at each step. 8 angular steps of 45 degrees provided optimised imaging performance in this study. Acquisition time is dependent on the total number of acquired waveforms. For example, the acquisition of 112,000 waveforms over 8 views, took approximately 1.5 hours.
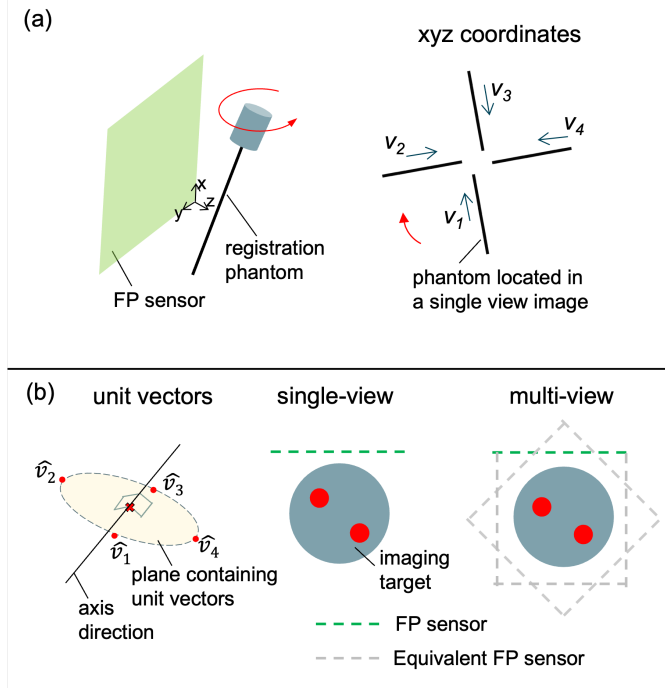
B. Multi-view image registration

Fig. 2. Multi-view sensor registration: The location of the axis is determined by imaging a registration phantom comprising a single optically absorbing hair strand. The phantom was rotated in 90-degree steps, to acquire PA images in four views. The lines lie on a one-sheeted hyperboloid, the axis of which is the rotation axis. To find this, the unit direction-vectors of the lines were fitted to a circle; the normal vector to the circle gives the direction of the axis (b). Finding any point on the axis will uniquely locate the axis, such as the centre of a circle fitted to the intersection of the four lines with a plane perpendicular to the axis. Equivalent FP sensors are synthesized by rotating the coordinates of the FP sensor around the axis; in the opposite direction to the phantom's rotation. The sensors are assigned time series acquired from the rotated target, in order to reconstruct an image.

The scanning of the FP sensor at each angular rotation of the target can be regarded as equivalent to placing eight 2-D ultrasound arrays around the target. In order to determine the positions of these notional arrays within a common coordinate system, a two-step registration procedure was developed (Fig. 2). Firstly, the location of the axis of rotation was determined with respect to the stationary FP sensor, as described below. Secondly, the positions of the arrays were found by rotating the coordinates of the FP sensor around the rotation axis, in angular steps equal to those of the target. The location of the rotation axis was determined by imaging a registration phantom consisting of a single straight strand of hair (Fig. 2a). The hair was imaged from four views in 90-degree steps. PA images of each view were reconstructed using a time reversal algorithim

[15], with the sound speed chosen to match water at the temperature measured inside the tank (1479m s^{-1}).

From the reconstructed images, the unit direction vector of the line phantom was obtained for each view. The unit vectors lie on a one-sheeted hyperboloid, the axis of which is the rotation axis. Fitting a circle to the vectors yields the unit direction vector of the axis, which is normal to the circle (Fig. 2b). To uniquely define the axis of rotation, a point on the axis must also be known. Such a point can be determined from the intersections of the reconstructed lines from the four views with a plane which has its normal along the axis. The intersections lie on a circle, the centre of which is a point on the axis. The coordinates of the arrays were subsequently determined by rotating the FP sensor coordinates around the axis, in the reverse direction to the target's rotation (Fig. 2b). By explicitly determining the axis of rotation, the registration procedure is robust to errors observed in pair-wise point cloud registration techniques[16] due to the presence of different limited-view artefacts in the registered pairwise single-view images.

C. Image reconstruction and visualisation

The time series recorded from the multiple views were combined to reconstruct a three-dimensional PA image using a two-sound speed, time reversal algorithm implemented using k-Wave [15,17]. For the mouse imaging studies, the raw photoacoustic signals were band-pass filtered between $0.3 - 7.5$ or 12.5 MHz to maximise SNR. The time series were corrected for acoustic attenuation in tissue using a time variant filtering method [18]. To implement dual sound speed reconstruction, the 3D computational grid, which had a voxel size of 40 or 50μm, was subdivided into two regions; one region containing water and another containing the imaging target. The target-containing region was identified from a prior photoacoustic image reconstructed assuming a single homogenous sound speed. The sound speed in the water region was chosen to match that of water at the temperature measured inside the imaging tank, while the sound speed inside the target (1540m s^{-1}) was selected using an autofocus approach, based on a metric of image sharpness [19]. After reconstruction, an approximate first order exponential correction for optical attenuation was applied radially [20]. The reconstructed images were displayed as maximum intensity projections (MIPs) using a logarithmic image intensity scale. No further image processing steps, such as vessel filtering or contrast histogram equalisation, were employed.

D. Phantom imaging

Two phantoms were constructed to evaluate the multi-view scanner and compare its performance to a single-view scanner. The first phantom was used to estimate the spatial resolution. It consisted of two optically clear fishing lines (100μm nominal diameter), marked at approximately equally-spaced intervals with a thin layer of black ink to create a sequence of optical absorbers. The lines were arranged in a cross-hair pattern. The second phantom consisted of 12 tubular agar inclusions made with a dilution of
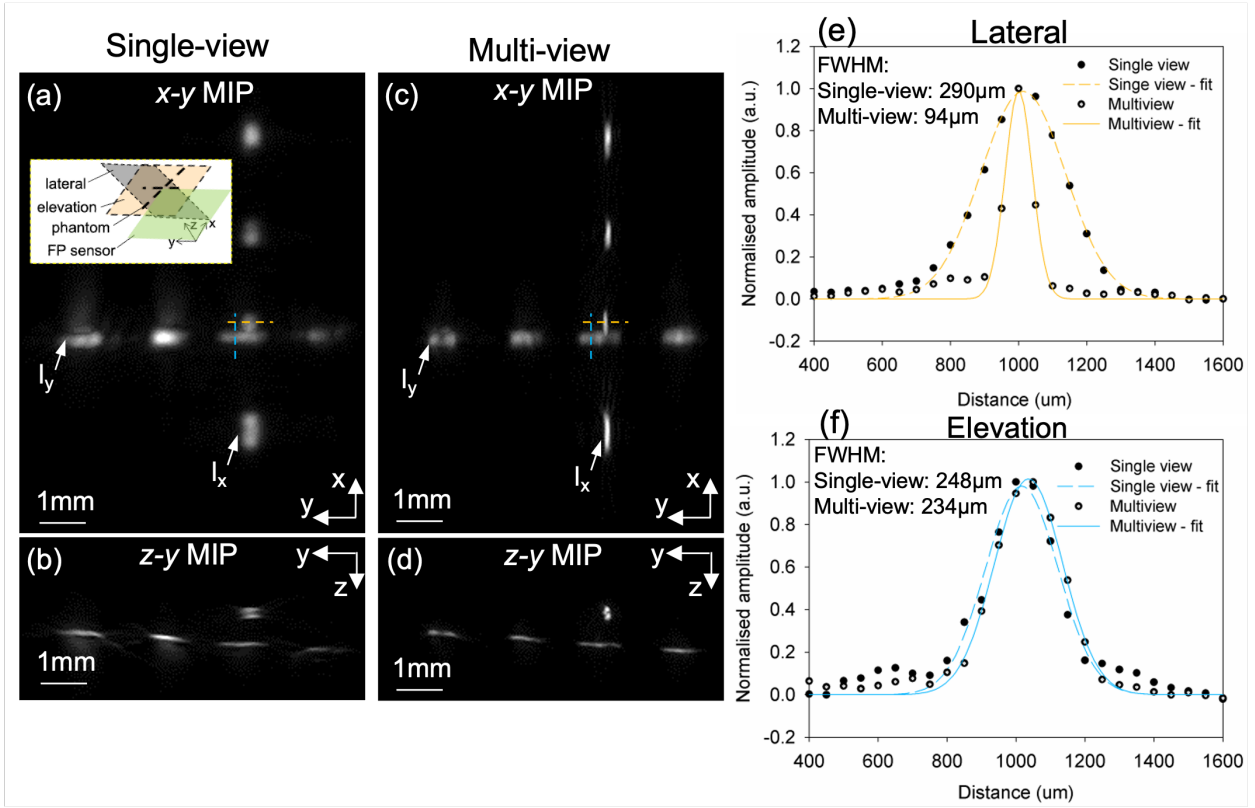
Fig. 3. System characterisation: Photoacoustic images of a phantom made up of two clear fishing lines (diameter ~100 um) marked with black ink to form a sequence of optical absorbers and arranged as a cross-hair. The lines, l_y and l_x, lie on the lateral and elevational planes respectively (inset figure a). The phantom is located ~12 mm from the FP sensor. The scanned x-y area on the sensor is 14 mm x 10 mm (in 100 um steps). PA images, reconstructed with sound speed of 1480m s^{-1} are shown as x-y and y-z maximum intensity projections (MIP) for single-view (a, b) and multi-view (c, d). Line l_x is noticeably sharper in the multi-view images, while the sharpness of l_y appears similar, although limited view artefacts are evident in the single-view images. (e, f) Normalised image intensity and Gaussian fit to profiles taken across l_x and l_y (at the locations indicated by the orange and blue lines respectively). (e) The lateral FWHM of the multi-view (94 mm) is 3 times lower than the single-view (290 mm), because the multi-view provides full-view of the acoustic field in-plane (f) The elevational FWHM of the multi-view (234 mm) is comparable to the single-view (248 mm), because it is primarily determined by the x-dimension scanned on the sensor (14 mm), which is the same for single-view and multi-view

india ink, inside a cylindrical background of 3% agar in a glycerine/water solution, mimicking the ultrasound properties of human tissue [21]. The absorption coefficient of the agar inclusions was 1 mm^{-1}, which is similar to oxygenated blood at the excitation wavelength of 700nm used. The diameters of the inclusions and the agar background were approximately 1mm and 24mm respectively, with the latter chosen to be comparable to the typical anatomical cross-sectional diameter of a mouse.

E. Mouse imaging

To demonstrate the performance of the multi-view scanner for whole body mouse imaging, PA images of ex-vivo mice were acquired. Three female nude mice (nu/nu CD1), 4-6 weeks old, were imaged after humane culling with an overdose of anesthetic. To minimize post-mortem changes in vasculature, a different mouse was used to demonstrate imaging of the head, thorax and abdominal regions. The mouse was placed in the custom sample holder described above. By adjusting the height of the sample holder in the water tank, the anatomical region to be imaged is placed adjacent to the sensor. The experiments were approved by a local ethical review panel at University College London and were performed in accordance with the UK Home Office Animals Scientific Procedures Act (1986).

III. RESULTS

PA images reconstructed from single-view and multi-view imaging of the cross-hair resolution phantom are shown in Fig. 3a-d. The images are presented as 2D x-y and z-y maximum intensity projections (MIP) of 3D datasets. The x-y plane is the elevational plane, while z-y is the lateral plane. From inspection, line l_x appears sharper in the multi-view images (Fig. 3c-d), than in the single-view images (Fig. 3a-b), suggesting a higher lateral resolution in the multi-view. The sharpness of line l_y, appears similar in both sets of images, despite the visible artefacts in the single-view images. To quantify the resolution, profiles were taken across the images, at locations indicated by the solid and dashed yellow lines. The full-width-half maxima (FWHM) of Gaussian fits to the data provide estimates of the lateral and elevational resolution respectively. Fig. 3e shows the lateral resolution of the multi-view (94 μm) is improved by a factor of three times over the single-view (290 μm). This is because multi-view imaging collects data from all angles, providing a full view of the acoustic field in-plane. Consequently, the lateral FWHM is approximately equal to the nominal diameter of the phantom

(100 μm). On the other hand, both single-view and multi-view have the same limited-view of the acoustic field in the elevation
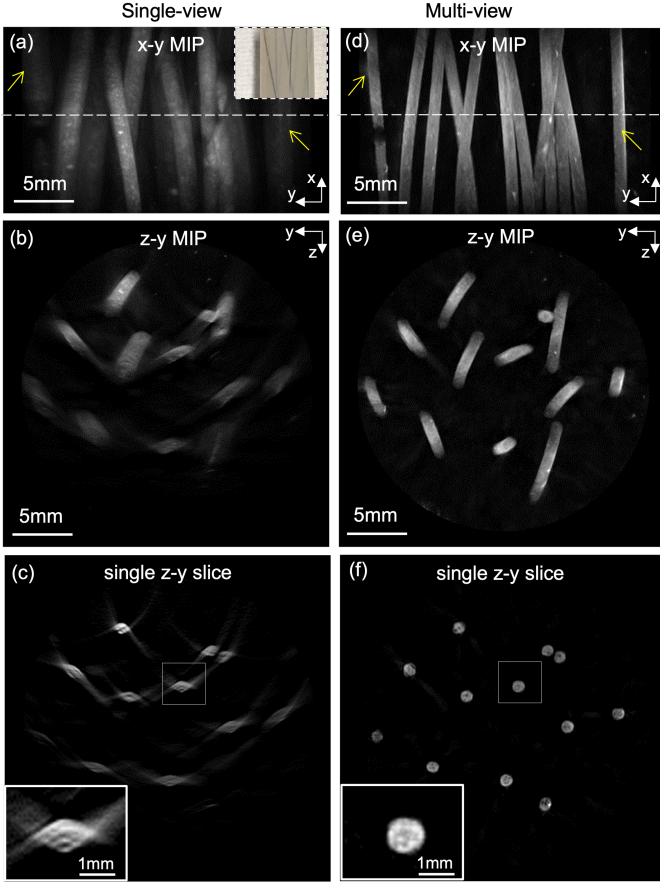

Fig. 4. PA imaging of a tissue mimicking phantom acquired at an excitation wavelength of 700nm. The phantom (inset figure a) consist of a cylindrical 3% agar background (diameter 24mm) and 12 black tubular inclusions (diameter 900um) with an absorption coefficient of 1mm^{-1}. **(a, d)** *x-y* MIP for single-view (a) and multi-view (d). Inclusions close to the edge of the field-of-view (indicated with yellow arrows) which are not clearly visualised in the single-view image are clear in the multi-view image; all 12 inclusions are noticeably sharper in the multi-view image. **(b, e)** *z-y* MIP for single-view (b) and multi-view (e) illustrating the complex 3D geometry of the tubes which are not oriented in a 2D plane. The deeper lying inclusions are less visible in the single-view image whereas all inclusions are equally visible in the multi-view. **(c, f)** *z-y* slice for single-view (c) and multi-view (f), taken at locations indicated by dashed lines in (a) and (d). In the single-view image, the expected circular cross-section of the inclusions appears oval-shaped, with visible wing-shaped limited-view artefacts. The inset image shows a close-up of the inclusion located within the dashed rectangle. In the multi-view image (f), the cross sections of the inclusions are accurately reconstructed, seen most clearly in the close-up inset image.

direction, determined by the dimension of the sensor scanned in the x-direction (14 mm). This results in similar FWHM in the elevation direction; 234 μm for multi-view and 248 μm for single-view (Fig. 3f). The dependence of the resolution on the sensor aperture can be observed in the single-view image, where the scanned x and y-dimensions on the sensor are 14mm and 10mm respectively. Consequently, a larger proportion of the wavefront emitted from l_y is detected, compared to l_x. This results in a smaller FWHM in the x-direction (vertical, 248 μm) than the y-direction (lateral, 290um).

After establishing the resolution of the multi-view scanner, PA images of a tissue mimicking agar phantom were acquired using single-view and multi-view acquisitions. These are shown as *x-y* MIPs (Fig. 4a, 4d), *y-z* MIPs (Fig 4b, 4e), and a single y-z slice (Fig 4c, 4f) taken at the location indicated by the dashed line in Fig 4a and Fig. 4d. In the single-view x-y MIP (Fig. 4a), all 12 tubes can be identified, although the tubes at the edge of the FOV highlighted with yellow arrows have very weak contrast. Deeper lying tubes have weak contrast compared to those closer to the sensor (y-z MIP, Fig. 4b). In addition, a single slice cross sectional view of the tubes reveals severe limited-view reconstruction artefacts in the single-view (Fig, 4c). All the tubes appear oval-shaped, instead of circular, and wing-shaped limited-view artefacts can be observed. This is best seen in the inset figure, which is a close-up of the tube indicated by the dashed line. In comparison to the single-view images, the tubes in the multi-view MIPs (Fig. 4d & 4e) have high contrast which is location-independent. The tubes are also noticeably sharper than their single-view counterparts. Furthermore, the reconstructed tubes have the expected circular cross section shape (Fig. 4f) indicating that the limited-view artefacts have been suppressed. The inset image in Fig. 4f, shows the cross-sectional dimension of a reconstructed tube approximates the nominal diameter of 1mm. These results demonstrate the multi-view scanner provides high contrast imaging without limited-view artefacts, over a sufficiently large FOV for small-animal imaging.

To evaluate the suitability of the scanner for whole-body small animal imaging, multi-view PA images of the abdominal region of a mouse were acquired and compared to single-view. The images are shown as *x-y* MIPs in Fig. 5. To aid visualisation of deeper lying anatomical features, the reconstructed volume was subdivided into posterior and anterior regions of the anatomy. The posterior region, which contains the spine, is adjacent to the FP sensor, while the anterior aspect is furthest away from the sensor. In the single-view image of the posterior region (Fig. 5a), the left and right kidney (lk, rk) are visible either side of the spine (sp). Ribs (r) connected to the spine are also visible at the top of the image. For comparison, in the corresponding multi-view image (Fig. 5b), additional anatomical structures such as parts of the spleen (sp), liver (l) and gastro-intestinal tract (gi), are also visible. In the single-view image of the anterior region (Fig. 5c), there are no discernible anatomical features despite the detectable image contrast. This is because the limited-view and the heterogeneous sound speed combine to blur-out features which are far away from the sensor. In contrast, the multi-view image (Fig. 5d) clearly shows lobes of the liver (l), part of the spleen (s) and an extensive gastro-intestinal tract (gi). To further aid visualisation, depth colour-coded MIPs of the multi-view images are shown in Fig. 6a and Fig 6b. The depth of the features can be referenced to the colour scale on the right of the image, with red being the most superficial and green to turquoise showing deeper lying anatomical features. Additional anatomical structures can be seen in the depth colour-coded *x-z* MIPs which were obtained by subdividing the dataset into the left and right lateral regions (Fig. 6c. and Fig. 6d. respectively). The entire spleen (s) is visible, along with part of the liver (l), left kidney (lk) and gastro-intestinal tract (gi). Taken together,
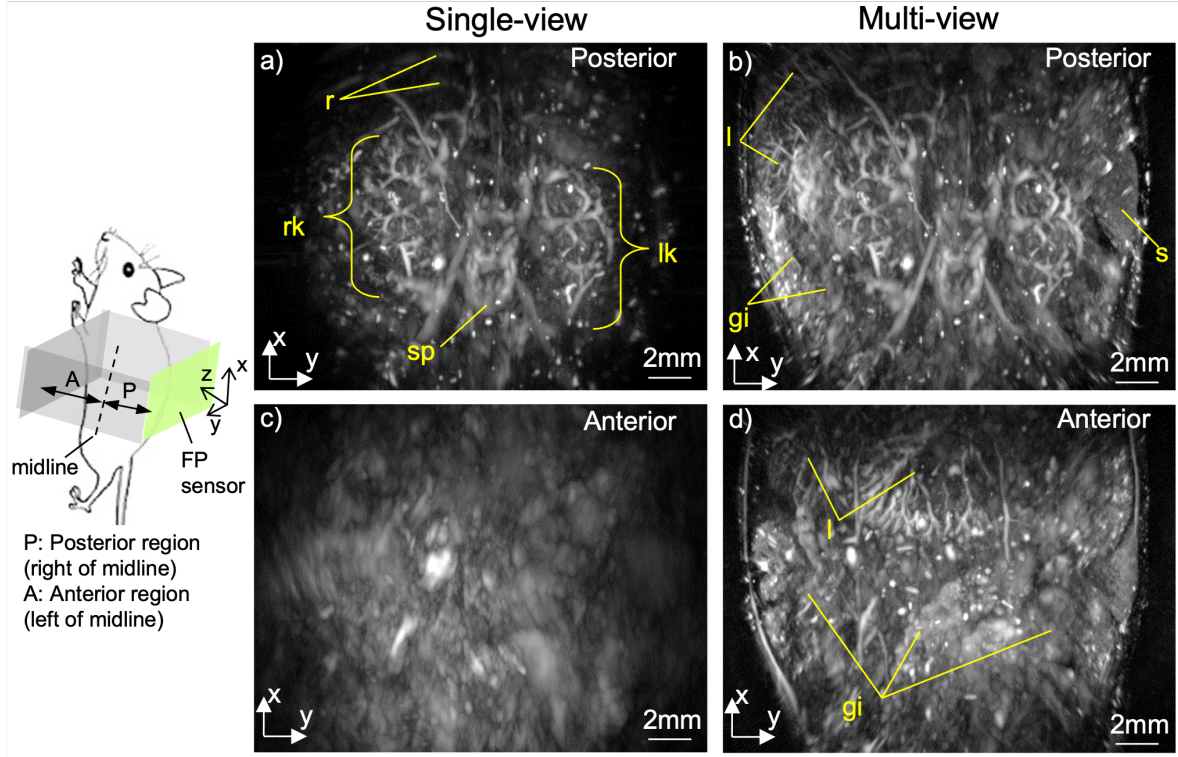
Fig. 5. Multi-view PA imaging of an ex-vivo mouse abdomen acquired at an excitation wavelength of 800nm**.** The images are shown as 2D *x-y* MIPs of 3D volumes. The reconstructed volume is subdivided into volumes containing the anterior and posterior region of the anatomy. **(a)** Single-view MIP of the posterior region. Visible anatomical features include ribs (r), right kidney (rk), left kidney (lk), spine (sp). **(b)** Multi-view MIP of the posterior region. In addition to the features visible in the single-view, the liver (l), spleen (s) and part of the gastrointestinal tract are visible in the multi-view. **(c)** Single-view MIP of the anterior region. There are no discernible anatomical features despite the detectable contrast, because PA signals are recorded from only one side of the mouse. **(d)** Multi-view MIP of the anterior region. In contrast to the single-view, anatomic features are accurately reconstructed, including the liver (l) and an extensive network of the gastrointestinal tract (gi). By detecting acoustic waves on all sides of the mouse, the multi-view scanner increases the FOV over which anatomical features can be reconstructed.
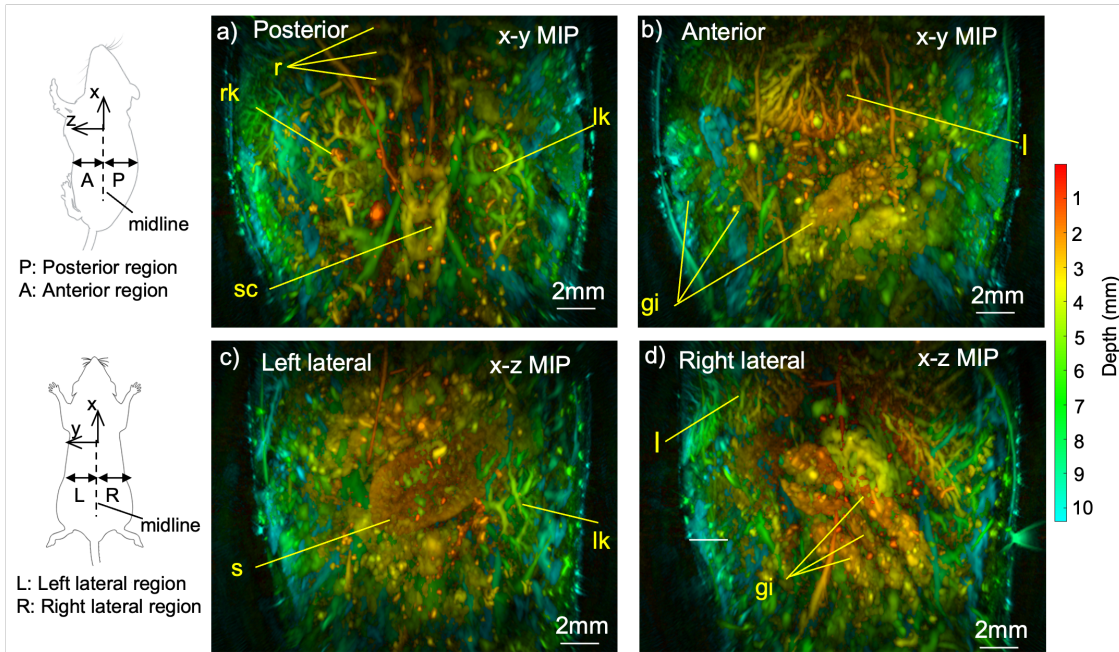

Fig. 6. Depth colour coded MIPs of multi-view PA image dataset of a mouse abdomen shown on Fig. 5**.** The reconstructed volume is subdivided into volumes containing the anterior and posterior region, or left and right lateral of the anatomy. Visible anatomical features include ribs (r), right kidney (rk), left kidney (lk), spine (sp). liver (l), spleen (s) and the gastrointestinal tract (gi). The depth of the features can be referenced to the colour scale on the right of the image, with red being the most superficial and green to turquoise showing deeper lying anatomical features
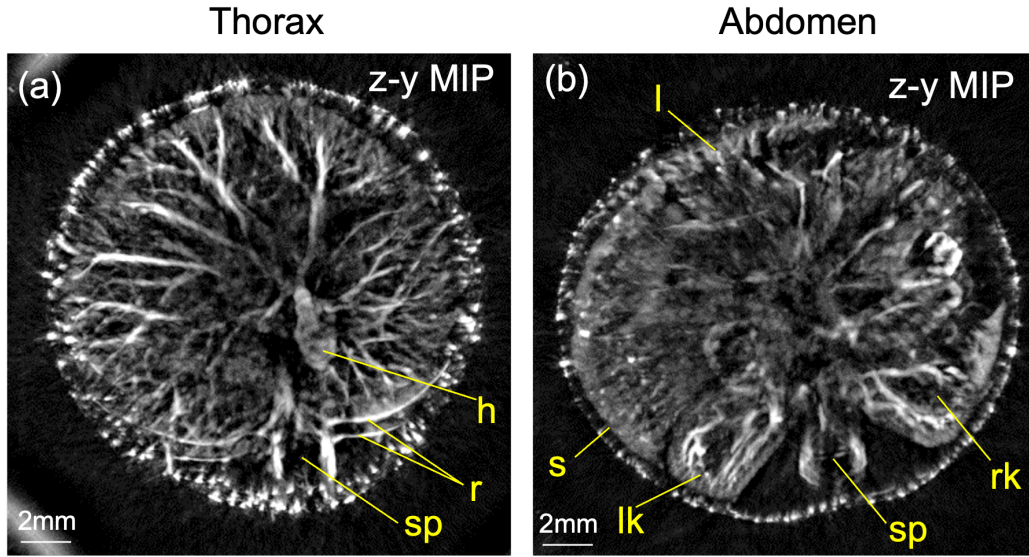
Thorax

Abdomen

Fig. 7. Multiview PA imaging: Cross sectional 2D *z-y* MIP of 3D volumes containing thoracic (a) and abdominal (b) region of a mouse. The thicknesses of the volumes are 3mm and 5mm respectively. The images were acquired at an excitation wavelength of 788nm. Visible anatomical features include Heart (h), ribs (r), spine (sp), liver (l), spleen (s), left kidney (lk), right kidney (rk). The two volumes were taken from a larger 3D dataset with a volume thickness of 14mm. A flythrough movie of the complete dataset, as well as a volume-rendered 3D movie can be viewed online (Supplementary movie 1 and 2).
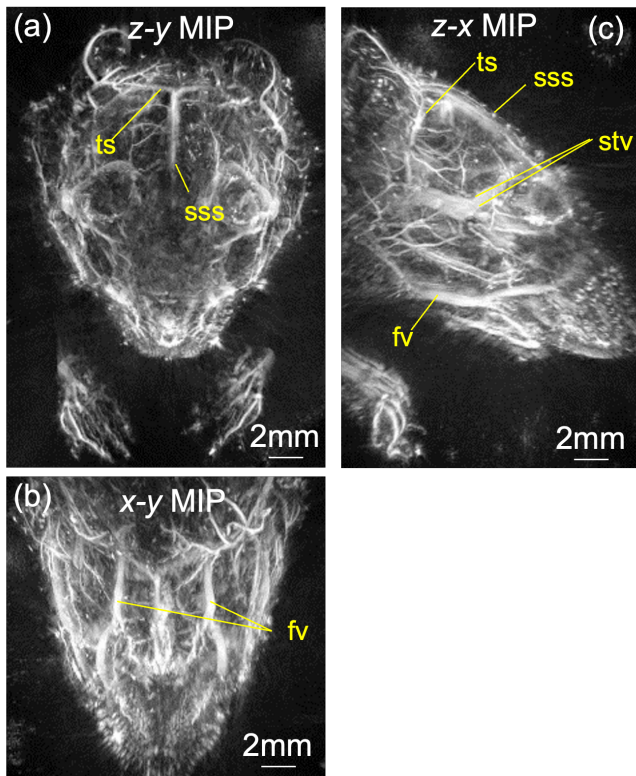

Fig. 8. Multi-view imaging of a mouse head acquired at an excitation wavelength of 700nm shown as z-y MIP (a), x-y MIP (b) and z-x MIP (c). Major blood vessels which can be identified include the superior sagittal sinus (sss), transverse sinus (ts), facial veins (fv) and superficial temporal veins (stv). Orbital, metatarsal and whisker pad vasculature help identify the eyes, fore paws and whiskers respectively.

the results in Fig. 5 and Fig. 6 illustrate how multi-view extends the FOV over which anatomical features can be accurately reconstructed, compared with the single-view.

To further illustrate the capability of the multi-view scanner, additional multi-view images of a mouse were acquired. A volume encompassing the thorax and upper abdomen was imaged. Two cross-sectional y-z MIPs taken from the reconstructed data are shown in Fig. 7. In Fig. 7a, the thickness of the MIP in the x-direction is approximately 3mm. Visible anatomical features include the spine (sp), ribs(r) and heart (h). A network of blood vessels is also visible across the entire cross section of the mouse. In Fig. 7b, the thicknesses of the MIP in the x-direction is approximately 5mm. The left kidney (lk), right kidney (rk), spleen (s), spine (sp), liver (l) can be visualised. To fully visualise the three-dimensional nature of the dataset, a fly-through movie (from the thorax to the abdomen) and a volume rendered 3D movie can be viewed online (Supplementary movie 1 and 2 respectively).

Additional multi-view images of the mouse head were acquired to illustrate multi-view imaging of blood vessels over a large FOV. These are shown in Fig. 8 as z-y, z-x and x-y MIPs of the 3D volume. Major blood vessels which can be identified include the superior sagittal sinus (sss), transverse sinus (ts), facial vein (fv) and the superficial temporal vein (stv). In addition, vasculature around the eyes, forepaws and whisker-pad can also be visualised in the images. A fly-through movie of the dataset can be viewed online (Supplementary movie 3)

IV. DISCUSSION AND CONCLUSIONS

In this study, a multi-view FP based scanner has been constructed for whole-body small animal imaging. The performance of the scanner has been demonstrated by the acquisition of high resolution, 3-D images of the mouse head,

thorax and abdomen, and visualising anatomical details across the mouse cross section with high quality. The measured resolution of the scanner was found to be <100μm (lateral) and <235μm (elevation). In reality, this represents a conservative estimate of the actual resolution, because the diameter of the phantom used to determine the FWHM was not small enough to approximate a spatial delta function. Moreover, the elevational resolution can be improved by increasing the scan aperture in the elevational direction (14mm in the current study), in order to increase the solid angle over which PA waves can be captured [11].

A distinguishing feature of this study is the implementation of a full 3-D tomographic image reconstruction using > 100,000 PA time series recorded at evenly spaced detection points around the mouse. This provides three main advantages over previous whole-body scanners. Firstly, by recording data from all sides of the mouse, the imaging depth limitation of scanners that record data from only one side of the mouse is overcome [4,5]. Secondly, because images are acquired with point-like detectors over the entire surface of the mouse, the poor elevational resolution and artefacts associated with stacking sub-images acquired with a ring array of weakly focused detectors are avoided [6,7]. Thirdly, the tomographic reconstruction using a large number of detection points provides a SNR gain, due to the signal averaging effect of the reconstruction when using the same data recorded by multiple detectors.

In contrast to whole-body scanners based on piezoelectric sensors, the scanner described in this study is based on the FP ultrasound sensor which offers significant advantages in terms of acoustic performance for PAT [11,12]. These include small element size and fine spatial sampling which enabled the near point-like sampling of the PA wavefield, thus avoiding the aliasing of high spatial frequencies, which is necessary for obtaining high resolution images. It also has a wide bandwidth and high sensitivity, which enabled the detection of broadband PA signals with high SNR. In comparison, an equivalent sized piezoelectric sensor will provide insufficient detection sensitivity, since the sensitivity scales with active area. If large elements are used to obtain adequate sensitivity, the directional response of the sensors risk compromising image quality due to image reconstruction artefacts. These factors enabled the scanner to record PA waves around the mouse with minimal distortion and high SNR. This, in combination with the use of a full 3-D tomographic reconstruction, enabled the reconstruction of high quality volumetric PA images without the need for post-processing image contrast enhancement steps such as adaptive contrast histogram equalisation and vessel filtering [6,7]. In the case of the latter, the implicit spatial priors imposed on the image reconstruction limits the range of anatomical features which can be visualised. It can also lead to hallucination of vessel-like artefacts, especially in bulk tissue [22].

The multi-view FP scanner enabled imaging across the whole mouse in a manner not possible with a single-view FP scanner. In the single-view images of the mouse, anatomical features far from the sensor are detected with sufficient SNR but are indistinguishable. This suggests optical and acoustic attenuation are not the primary factors limiting whole-body imaging when PA signals are recorded only on one side of the

mouse. Rather, it is the combined distorting effect of limited-view artefacts and aberration of the PA waves due to sound-speed heterogeneities, which prevent single-view imaging of the whole mouse. In contrast, by detecting PA signals from different angles around the mouse, the multi-view scanner provides a full-view of the PA wavefield. It also means that the strongest signal detected from any particular source will have taken the shortest path to reach the sensor, thereby minimising sound-speed heterogeneity induced wavefront aberrations which scale with acoustic propagation distance.

Although the described scanner illustrates the concept of full-view whole-body small animal imaging, it is not suitable in its current form for *in-vivo* imaging due to the long acquisition time (~1.5 hrs). This is due to the use of a single focussed beam to interrogate the sensor and the low repetition rate of the excitation laser. However, it has been demonstrated that this limitation can be addressed by parallelizing the detection and using a high repetition rate laser as described in reference [23]. This approach would enable the acquisition of a single view image in 1.2s, assuming the same number of detection points as the current study. Multi-view acquisition could then be achieved in <20s (including rotation time of the stage at a speed of 50 degrees/second), which is comparable to previous piezoelectric based whole-body scanners [10,24]. A second limitation of the current study is the rotation of the target relative to a stationary FP sensor to achieve multi-view imaging. This makes it susceptible to potential motion errors, such as during in-vivo imaging. It also introduces complexity in terms of incorporating an anaesthesia delivery system for the mouse as it rotates. This limitation could be addressed by keeping the target stationary, while the FP scanner is mounted on a rotating gantry or by using of multiple FP sensors which avoids the need for rotation. A second-generation version of the scanner suitable for in-vivo imaging could combine multi-beam sensor interrogation with multi-sided FP sensors to achieve fast (<10s) whole-body imaging, without rotating the mouse.

In summary, this study has presented a multi-view FP-based scanner which enabled the acquisition of high-resolution, high-fidelity three-dimensional whole-body images of a mouse, with anatomical features visible across the entire cross section.

REFERENCES

[1] J. Xia. and L.V. Wang, "Small-animal whole-body photoacoustic tomography: a review," *IEEE Trans. Biomed. Eng.* **61**, 1380–9 (2014).

[2] P. Beard, "Biomedical Photoacoustic Imaging," *Interface Focus* **1**, 602–631 (2011).

[3] R. B. Lam *et al.,* "Dynamic optical angiography of mouse anatomy using radial projections," in *Proceedings of SPIE* vol. 7564 Vol 7564 (2010).

[4] Y. Asao *et al.,* "In Vivo Label-Free Observation of Tumor-Related Blood Vessels in Small Animals Using a Newly Designed Photoacoustic 3D Imaging System," *Ultrason. Imaging* **44**, 96–104 (2022).

[5] J. J. Gateau, M. A. Caballero, A. Dima, and V. Ntziachristos, "Three-dimensional optoacoustic tomography using a conventional ultrasound linear detector array: Whole-body tomographic system for small animals," *Med. Phys.* **40**, 013302 (2013).

[6] L. Li *et al.,* "Single-impulse panoramic photoacoustic computed tomography of small-animal whole-body dynamics at high spatiotemporal resolution,". *Nat. Biomed. Eng.* **1**, (2017).

[7] E. Merčep, J. L. Herraiz, X. L. Deán-Ben, and D. Razansky, "Transmission–reflection optoacoustic ultrasound (TROPUS) computed tomography of small animals," *Light Sci. Appl.* **8**, (2019).

[8] R. A. Kruger, W. L. Kiser, D. R. Reinecke, G. A. Kruger, and K. D. Miller, "Thermoacoustic Molecular Imaging of Small Animals. *Mol. Imaging,*" **2**, 113–123 (2003).

[9] H. P. Brecht *et al.,* "Whole-body three-dimensional optoacoustic tomography system for small animals," *J. Biomed. Opt.* **14**, 064007 (2009).

[10] X. L. Deán-Ben, T. F. Fehm, S. J. Ford, S. Gottschalk, and D. Razansky, "Spiral volumetric optoacoustic tomography visualizes multi-scale dynamics in mice," *Light Sci. Appl.* **6**, e16247–e16247 (2017).

[11] E. Zhang, J. Laufer, and P. Beard, "Backward-mode multiwavelength photoacoustic scanner using a planar Fabry-Perot polymer film ultrasound sensor for high-resolution three-dimensional imaging of biological tissues,". *Appl. Opt.* **47**, 561–577 (2008).

[12] A. P. Jathoul *et al,* "Deep in vivo photoacoustic imaging of mammalian tissues using a tyrosinase-based genetic reporter," *Nat. Photonics* **9**, 239–246 (2015).

[13] J. Laufer *et al,* "In vivo photoacoustic imaging of mouse embryo," *J. Biomed. Opt.* **17**, 061220 (2012).

[14] O. Ogunlade *et al,* "In vivo three-dimensional photoacoustic imaging of the renal vasculature in preclinical rodent models," *Am. J. Physiol. Physiol.* **314**, F1145–F1153 (2018).

[15] B. E. Treeby, E. Z. Zhang and B. T. Cox, "Photoacoustic tomography in absorbing acoustic media using time reversal," *Inverse Probl.* **26**, 115003 (2010).

[16] R. Ellwood, F. Lucka, E. Z. Zhang, P. C. Beard and B. T. Cox, "Photoacoustic imaging with a multi-view Fabry-Pérot scanner" *Proc SPIE* **10064**, 1–7 (2017).

[17] B. E. Treeby and B. T. Cox, "k-Wave: MATLAB toolbox for the simulation and reconstruction of photoacoustic wave fields," *J. Biomed. Opt.* **15**, 021314 (2010).

[18] B. E. Treeby, "Acoustic attenuation compensation in photoacoustic tomography using time-variant filtering," *J. Biomed. Opt.* **18**, 036008 (2013).

[19] B. E. Treeby, T. K. Varslot, E. Z. Zhang, J. G. Laufer and P. C. Beard, "Automatic sound speed selection in photoacoustic image reconstruction using an autofocus approach," *J. Biomed. Opt.* **16**, 090501 (2011).

[20] B. E. Treeby, J. Jaros and B. T. Cox, "Advanced photoacoustic image reconstruction using the k-Wave toolbox," in *Proceedings of SPIE* (eds. Oraevsky, A. A. & Wang, L. V.) vol. 9708 97082P (2016).

[21] R. M. Souza *et al.,* "Standard operating procedure to prepare agar phantoms," *J. Phys. Conf. Ser.* **733**, 012044 (2016).

[22] A. Longo *et al.,* "Assessment of hessian-based Frangi vesselness filter in optoacoustic imaging," *Photoacoustics* **20**, 100200 (2020).

[23] N. T. Huynh *et al.,* "A fast all-optical 3D photoacoustic scanner for clinical vascular imaging." *Nat. Biomed. Eng.* 1-18, (2024) .

[24] L. Lin *et al.,* "High-speed three-dimensional photoacoustic computed tomography for preclinical research and clinical translation," *Nat. Commun.* **12**, 882 (2021).